UC Davis

UC Davis Previously Published Works

Title

Aeroacoustic Analysis of a Lift-Offset Coaxial Rotor Using High-Fidelity CFD/CSD Loose Coupling Simulation

Permalink

https://escholarship.org/uc/item/3s93w7s6

Journal

Journal of the American Helicopter Society, 65(1)

ISSN

0002-8711

Authors

Jia, Zhongqi

Lee, Seongkyu

Sharma, Kalki

et al.

Publication Date

2020

DOI

10.4050/jahs.65.012011

eScholarship.org Powered by the California Digital Library
University of California

Aeroacoustic Analysis of a Lift-Offset Coaxial Rotor Using High-Fidelity CFD/CSD Loose Coupling Simulation

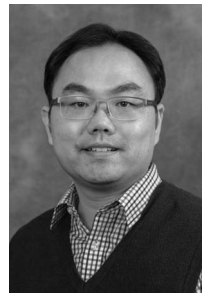

Zhongqi (Henry) Jia* — *Ph.D. Student*
Seongkyu Lee — *Assistant Professor*
University of California, Davis, CA

Kalki Sharma — *Ph.D. Student*
Kenneth S. Brentner — *Professor*
The Pennsylvania State University, University Park, PA

This paper presents the aeroacoustic analysis of a lift-offset coaxial rotor in high-speed forward flight using the high-fidelity computational fluid dynamics/computational structural dynamics (CFD/CSD) loose coupling software Helios. Acoustic simulations are performed using the software PSU-WOPWOP at eight microphones positioned below the coaxial rotor. The total power of the three speed cases—100, 150, and 200 kt—is validated against flight-test data and shows good agreement. A series of parametric studies is also conducted to investigate the effect of lift offset, flight speed, and rotor-to-rotor separation distance on acoustics of the coaxial rotor. Strong blade-crossover and self-blade–vortex interaction events of the coaxial rotor, which are major sources of loading noise, are captured via high-fidelity CFD simulations in all speed cases. Highly impulsive acoustic pressure signals are identified in all simulation cases, and the magnitude of mid-frequency sound pressure level (SPL) increases significantly with increasing flight speed and lift offset. The strength of mid-frequency SPL, on the other hand, is reduced significantly as the rotor-to-rotor separation distance increases at 100 kt. However, the higher speed cases do not show a significant reduction in mid-frequency SPL with increasing separation distance.

Nomenclature

C_{tip}	tip chord length, m
c	speed of sound in the undisturbed medium, m/s
d	distance to the nearest wall, m
dF_z	blade sectional normal force, N/m
$dF_z/d\Omega$	azimuthal (time) derivative of F_z, N/(m-deg)
L_{ref}	grid unit reference length, m
$\vec{l}$	blade surface loading vector, N/m
l_r	blade surface loading in the radiation direction, $\vec{l}\cdot\hat{r}$, N/m
$\dot{l}_r$	change of blade surface loading in the radiation direction with respect to the acoustic source emission time, $(\partial\vec{l}/\partial\tau)\cdot\hat{r}$, N/(m-s)
$\vec{M}$	local Mach number vector
M_{AT}	advancing-tip Mach number
M_r	Mach number of the blade surface in the radiation direction, $\vec{M}\cdot\hat{r}$
M_∞	freestream Mach number
P_{lower}	lower rotor power, hp
P_{total}	total power of the vehicle, hp
P_{upper}	upper rotor power, hp
p'	total acoustic pressure, Pa
p'_L	loading noise acoustic pressure, Pa
p'_T	thickness noise acoustic pressure, Pa
Q	Q-criterion, $1/\text{s}^2$
$\bar{Q}$	nonscaled Q-criterion, $Q/(c/L_{\text{ref}})^2$
R	rotor radius, m
r	distance between $\vec{y}$ and $\vec{x}$, m
$\hat{r}$	unit vector in the radiation direction
r_b	radial position of the blade, m
S_{ij}	strain-rate tensor, $1/\text{s}^2$
T	total rotor thrust, N
T_{aux}	auxiliary engine thrust, hp
u^*	friction velocity, $\sqrt{\tau_w/\rho_o}$, m/s
V_∞	freestream velocity, kt
W_{ij}	spin-rate tensor, $1/\text{s}^2$
$\vec{x}$	observer position, m
y^+	dimensionless wall distance, u^*d/ν_{vis}
$\vec{y}$	sound source position, m
ΔM_x	differential rolling moment between the upper and lower rotors, N-m
η	propeller propulsive efficiency
μ	advance ratio
ν	local fluid velocity on the blade surface, m/s
ν_n	normal component of fluid velocity, m/s
ν_{vis}	air viscosity, m^2/s
ρ_∞	air density in the undisturbed medium, kg/m^3
τ_w	wall shear stress, Pa
Ψ	rotor azimuth, deg
Ω	rotation rate, RPM

Subscript

ret	evaluated at the retarded time

*Corresponding author; email: jia@ucdavis.edu.
Presented at the AHS International 74th Annual Forum & Technology Display, Phoenix, AZ, May 14–17, 2018. Manuscript received September 2018; accepted August 2019.

 © 2020 AHS International

Introduction

High-speed forward flight capability is a key design requirement for modern military rotorcraft. However, the forward flight speed of a conventional rotorcraft design is always limited due to an aerodynamic barrier, known as retreating blade stall. During retreating blade stall, the retreating side of the rotor disk can no longer produce additional integrated lift to counterbalance the advancing-side rolling moment, as the angle-of-attack of the retreating blades reaches a critical value. In the 1970s, the Sikorsky Aircraft Corporation applied the Advancing Blade Concept (ABC) (Ref. 1) to the hingeless rotor system of a compound coaxial helicopter with auxiliary thrust engines. This helicopter, the XH-59A (see Fig. 1(a) (Ref. 2)), has achieved a maximum speed of approximately 260 kt in a dive: the fastest recorded helicopter speed at the time (Ref. 1). The primary advantage of the ABC rotor design is to optimize the lift potential on the advancing sides of a coaxial rotor and to minimize the adverse effects of retreating blade stall by reducing lift or the angle-of-attack on the retreating sides. This ABC strategy, or also known as the lift-offset rotor design, allows each rotor to produce greater integrated lift on the advancing side of the rotor disk and to carry an individual rolling moment of opposite direction and equal magnitude. The mathematical expression of lift offset (LO) is given as

$$\mathrm{LO} = \frac{\Delta M_x}{T \cdot R} \tag{1}$$

where ΔM_x is the differential rolling moment between the upper and lower rotors, T is the total rotor thrust, and R is the rotor radius. Multiple studies (Refs. 3, 4) have validated the ABC rotor design and its utilization of lift offset. The company made advancements on its original design and introduced the X2 Technology™ Demonstrator (see Fig. 1(b) (Ref. 5)) and S-97 Raider (see Fig. 1(c) (Ref. 6)) in the 2000s and 2010s, respectively.

The advantages of a lift-offset coaxial design have also been explored in previous research. Previous studies (Refs. 7–9) have shown that increasing the value of lift offset can further improve the maximum lift capacity as well as the power performance of a coaxial rotor. Owing to the potential performance benefits of a lift-offset coaxial rotor at high speed, the Joint Multi-Role Rotorcraft Technology Demonstrator (JMR-TD) program is currently considering a lift-offset coaxial design as one of the possible next-generation military rotorcraft (see Fig. 1(d) (Ref. 10)).

Though coaxial configurations utilizing lift offset have been capable of achieving high-speed forward flight, they have a potential risk of producing impulsive noise due to strong aerodynamic interactions, such as blade–vortex interactions (BVIs). BVI occurs when a blade–tip vortex interacts with a blade surface in close proximity. For a compound coaxial helicopter such as the XH-59A, where the rotor shaft does not need to be tilted forward to provide propulsive force, self-BVI (tip vortices interacting with the blades of the same rotor where they were generated) could occur at high speed and increase the severity of impulsive noise. Furthermore, Kim et al. (Ref. 11) discovered that rotor-to-rotor BVI (tip vortices from one rotor interacting with the other rotor) of a two-bladed lift-offset coaxial configuration can be an intensive acoustic source. Walsh et al. (Ref. 12) also analyzed the acoustics of a lift-offset coaxial configuration based on the XH-59A properties using the Rotorcraft Comprehensive Analysis System (RCAS) (Ref. 13) software and identified BVI-like acoustic signals. In 2017, Schatzman et al. (Ref. 14) performed research on a two-bladed coaxial model, which does not have lift offset, and observed abrupt changes of surface blade pressure induced by blade-crossover events. They speculated that this source could lead to impulsive noise.

Results from these aeroacoustic studies, however, are limited to low-fidelity simulation models. Neither Schatzman et al. nor Kim et al. have considered a modern three- or four-bladed lift-offset coaxial rotor for their studies. To the best of authors' knowledge, no one has utilized a first-principled and high-fidelity computational fluid dynamics/computational structural dynamics (CFD/CSD) loose coupling approach to predict lift-offset rotorcraft acoustics. In this paper, the acoustic characteristics of a three-bladed coaxial rotor are assessed based on high-fidelity CFD/CSD loose coupling simulations. Parametric studies are also performed to

(a) Sikorsky XH-59A (Ref. 2)

(b) Sikorsky X-2 (Ref. 5)

(c) Sikorsky S-97 Raider (Ref. 6)

(d) Conceptual drawing of SB > 1 Defiant (Ref. 10)

Fig. 1. Compound lift-offset coaxial rotors.

demonstrate the influence of physical parameters—forward flight speed, lift offset, and rotor-to-rotor separation distance—on the acoustics of a lift-offset coaxial rotor.

Method

A notional three-bladed lift-offset coaxial rotor of the XH-59A was modeled based on a publicly available technical report (Ref. 15) for this research, with the basic properties listed in Table 1. Since the airfoil data of the XH-59A are not publicly available, the following airfoils, which have matched the thickness distribution of the actual airfoils, were used: NACA-0026 was used for $r_b/R < 0.418$; NACA-63216 was used for $0.418 \leq r_b/R \geq 0.678$; NACA-23012 was used for $r_b/R > 0.678$. Blade chord, thickness, and twist distributions are shown in Fig. 2.

CFD mesh

The dual-mesh methodology, dividing the computational domain into near-body overset mesh and off-body Cartesian mesh, was implemented in this work. NASA's structured grid generation tool OVERGRID (Ref. 16), which is compatible with Chimera Grid Tools (Ref. 17), was used for the generation of near-body overset grids based on an O-grid topology (see Fig. 3(a)). Each blade is composed of three components: main blade, blade root, and blade tip. The dimensions of the main-blade grid are 267 (chordwise direction) × 189 (spanwise direction) × 65 (normal direction) points with leading and trailing edge spacings equal to 0.05% C_{tip} and 0.02% C_{tip}, respectively, where C_{tip} is the tip chord length. The dimensions of the root- and tip-cap grids are 118 × 121 × 65 points and 109 × 103 × 65 points, respectively. The grid dimensions were chosen based on the high-fidelity rotorcraft CFD simulations performed by Chanderjian (Refs. 18, 19). The initial and end spacing values in the normal direction of the volume grids are $5.0 \times 10^{-4}\%\ C_{\text{tip}}$ and 10% C_{tip}, with a dimensionless wall distance $y^+ = 1.0$, leading to approximately 5 million grid points per blade and 30 million grid points for all six blades.

The off-body Cartesian mesh (see Fig. 3(b)) was constructed by the adaptive off-body Cartesian solver SAMCart (Ref. 20) in Helios (Ref. 21), a high-fidelity rotorcraft simulation software being developed under the U.S. Department of Defense (DoD) Computational Research and Engineering Acquisition Tools and Environments-Air Vehicles (CREATE™-AV) program. Eight levels of adaptive mesh refinement (AMR) were used after the first-rotor revolution to resolve the rotor wake in the far field. The y- and z-boundaries of this AMR domain are $1.25R$ away from the origin. The boundaries in the x-direction are located at $-1.25R$ and $3.50R$. In addition to AMR, a small fixed refinement box that enclosed the coaxial rotor was specified to better capture near-body flow physics. The boundaries of this fixed refinement box are $0.26R$ away from the origin in the z-direction and $1.25R$ away from the origin in both the x- and y-directions.

Table 1. Basic properties of the XH-59A

Aircraft Properties	Given Information
Aircraft length	12.7 m (41.67 ft)
Aircraft height	2.4 m (8 ft)
Rotor radius (R)	5.5 m (18 ft)
Tip chord length (C_{tip})	0.29 m (0.94 ft)
Number of rotors	Two
Blades per rotor	Three
Rotation of the upper rotor	Counterclockwise
Rotation of the lower rotor	Clockwise
Vertical separation distance	0.76 m (2.5 ft)
Shaft tilt angle	0°
Nominal rotor speed	345 RPM
Nominal rotor tip speed	198 m/s (650 ft/s)
Gross weight	5398 kg (11,900 lb)
Power plants (lift)	Two PT6-3
Power plants (thrust)	Two J60-P3A

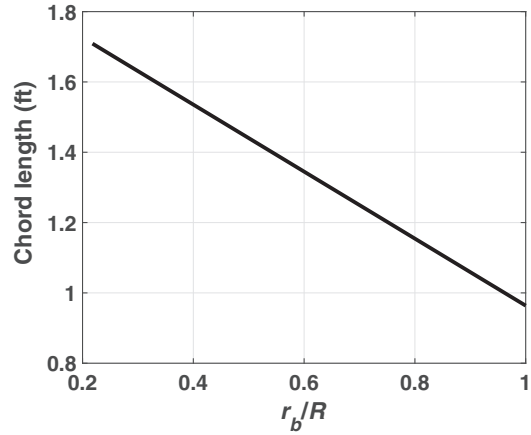

(a) Blade chord distribution

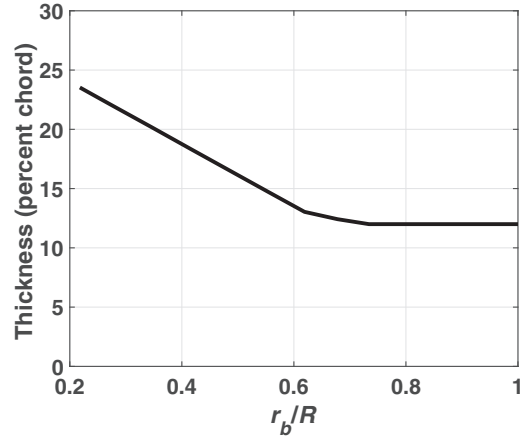

(b) Blade thickness distribution

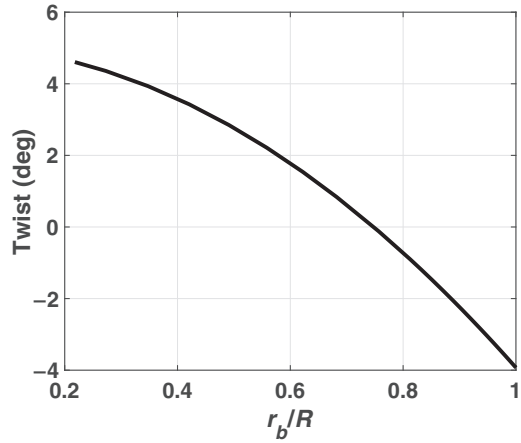

(c) Blade twist distribution

Fig. 2. Properties of the XH59-A rotor blade.

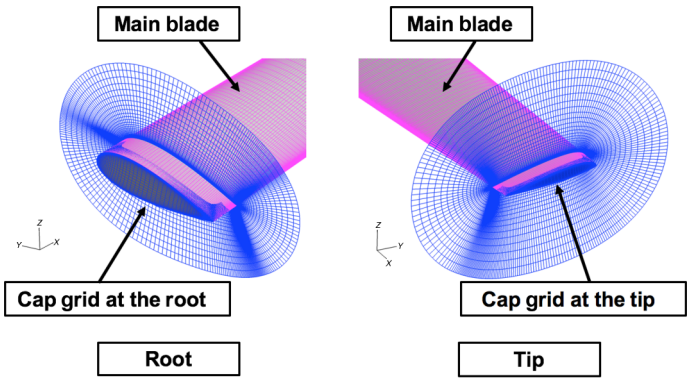

(a) Near-body grids

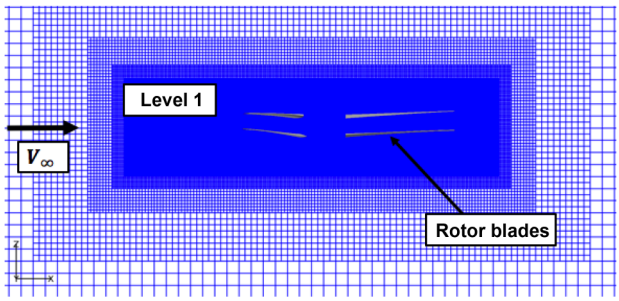

(b) Cartesian mesh

Fig. 3. Near- and off-body meshes.

The dimensions of the off-body domain are $20R$ away from the origin in each direction with the finest off-body spacing (level 1 mesh) equal to 10% C_{tip}. The total amount of off-body Cartesian grid points is approximately 76 million at the first time step and rises to approximately 130 million after the numerical convergence of simulation results. Neither the XH-59A fuselage nor the coaxial rotor hub is included in the CFD model.

CFD/CSD loose coupling simulation setup

CFD/CSD loose coupling simulations were achieved primarily using RCAS (the CSD and flight dynamics module), OVERFLOW (the near-body flow solver), and SAMCart (the off-body Cartesian flow solver) of Helios. First, the coaxial configuration was trimmed using RCAS based on six control variables—pilot collective, differential pilot collective, pilot lateral cyclic, differential pilot lateral cyclic, pilot longitudinal cyclic, and differential pilot longitudinal cyclic—for high-speed steady forward flight at an altitude of 3000 ft. Details regarding these control inputs can be found in the technical report (Ref. 15). The shaft angle-of-attack was fixed at 0° for the auxiliary propulsion mode of the XH-59A, that is, the coaxial rotor system only provided lift but no propulsive force; two auxiliary jet engines provided all the propulsive force in this operational mode. The vertical force was trimmed to balance the vehicle weight. The force equilibrium in the x-direction was achieved by balancing the rotor drag, fuselage drag, and forward auxiliary thrust. The fuselage drag coefficient was estimated based on a wind tunnel experiment (Ref. 22) of the XH-59A. Furthermore, the lift-offset value of the coaxial rotor as described in Eq. (1) was set by trimming the vehicle to a required differential rolling moment (M_x).

Following the rotorcraft trim, the numerical setup of near- and off-body flow solvers was established. In the present work, OVERFLOW (Ref. 23) and SAMCart of Helios were used to simulate near- and off-body flows. A fifth-order spatial scheme and a second-order temporal scheme were used for time-accurate CFD simulations in both near- and off-body grids. The detached eddy simulation (DES) (Ref. 25) coupled with the Spalart–Allmaras Reynolds-averaged Navier–Stokes turbulence model (Ref. 24) (SA-DES), and curvature-rotation correction built in OVERFLOW was employed for turbulence modeling. In the interest of BVI prediction, a time step size equal to 0.25° (degrees azimuth) yielding 1440 time steps per rotor revolution was used. The time step size was also chosen based on Chanderjian's research studies (Refs. 18, 19) of high-fidelity rotorcraft CFD simulations. Twenty and 10 dual-time-stepping subiterations within each time step were used for temporal convergence in both near-body and off-body calculations, respectively.

The frequency of the loose coupling simulation was set to every 180° after the first rotor revolution. Blade surface flow solutions and deformed geometries were extracted at every two time steps (0.5°) over the last rotor revolution for acoustic analysis. A detailed description of the CFD/CSD loose coupling approach can be found in the work written by Potsdam et al. (Ref. 26).

Acoustic simulation setup

PSU-WOPWOP (Refs. 27, 28), the acoustic simulation software developed at the Pennsylvania State University, was used to predict far-field noise. It utilizes a numerical implementation of Farassat's Formulation 1A (Refs. 29, 30) of the Ffowcs Williams and Hawkings equation (Ref. 31). The equations of Farassat's Formulation 1A can be written as

$$p'(\vec{x},t) = p'_T(\vec{x},t) + p'_L(\vec{x},t) \tag{2}$$

$$4\pi p'_T(\vec{x},t) = \int_{f=0}\left[\frac{\rho_\infty(\dot{v}_n + v_{\dot{n}})}{r|1-M_r|^2}\right]_{\text{ret}} dS + \int_{f=0}\left[\frac{\rho_\infty v_n(r\dot{M}_r + c(M_r - M^2))}{r^2|1-M_r|^3}\right]_{\text{ret}} dS \tag{3}$$

$$4\pi p'_L(\vec{x},t) = \frac{1}{c}\int_{f=0}\left[\frac{\dot{l}_r}{r|1-M_r|^2}\right]_{\text{ret}} dS + \int_{f=0}\left[\frac{l_r - l_M}{r^2|1-M_r|^2}\right]_{\text{ret}} dS + \frac{1}{c}\int_{f=0}\left[\frac{l_r(r\dot{M}_r + c(M_r - M^2))}{r^2|1-M_r|^3}\right]_{\text{ret}} dS \tag{4}$$

In this work, Farassat's Formulation 1A is calculated based on the impermeable surface strategy, and the quadrupole source is neglected.

Before the discussion of acoustic results, it is also important to review the key quantities in Eqs. (3) and (4). In Farassat's Formulation 1A, the term $1/|1-M_r|$ is known as the Doppler amplification factor (Ref. 12) and is dependent on both the magnitude of blade surface Mach number and the observer position. When an advancing blade with high tip Mach number moves toward an observer, a large value of $1/|1-M_r|$ will be reached, and thus the magnitude of loading noise is expected to increase. Furthermore, the quantity $\dot{l}_r$ in the first integral of Eq. (4), which is an indication factor of impulsive aerodynamic interactions (e.g., BVI), can also contribute significantly to loading noise. A combination of large $\dot{l}_r$ and $1/|1-M_r|$ can lead to intensive acoustic pressure signals. However, a large value for $\dot{l}_r$ or an abrupt change of airloads may not always yield impulsive acoustic signals if $1/|1-M_r|$ is small. Moreover, it should also be noticed that the second and third integrals of Eq. (4), when compared to the first integral of Eq. (4), are generally small in magnitude in the far field because of the term r^2. These two integrals are often considered as the near-field terms since they are more dominant in the near field.

Table 2. Microphone locations

Microphone Number	Position[a] (x,y,z)
1	(−5.00, 0.00, −1.00)
2	(−3.54, −3.54, −1.00)
3	(0.00, −5.00, −1.00)
4	(3.54, −3.54, −1.00)
5	(5.00, 0.00, −1.00)
6	(3.54, 3.54, −1.00)
7	(0.00, 5.00, −1.00)
8	(−3.45, 3.45, −1.00)

[a]Referenced from the mid point between the upper and lower rotor hubs in terms of rotor radius R.

Microphone positions

Eight microphones, each with a distance equal to approximately $5R$ from the midpoint between the upper and lower rotors, were used to identify the acoustic characteristics of the lift-offset coaxial rotor. The eight microphones are positioned on a circle parallel to the rotor planes and are also located one rotor radius below the midpoint. Their positions are shown in Table 2 in terms of the rotor radius R. Two schematic diagrams, which represent the microphone positions, are illustrated in Fig. 4.

Results

Three forward flight cases at 100, 150, and 200 kt were simulated and analyzed. The flight condition of each simulation case is displayed in Table 3. The M_{AT} at 200 kt was kept the same as the M_{AT} at 150 kt by reducing the rotor rotation rate to avoid highly nonlinear and compressible flow physics such as drag divergence and delocalization, which

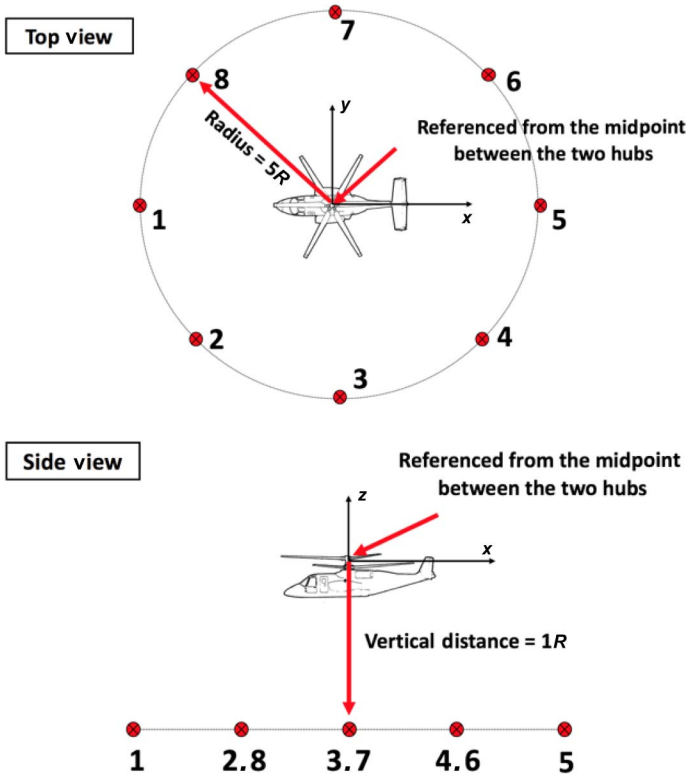

Fig. 4. Schematic representation of microphone locations.

Table 3. Flight conditions at 100, 150, and 200 kt

V_∞ (kt)	M_∞	M_{AT}	μ	Ω (RPM)
100	0.15	0.74	0.26	345
150	0.23	0.82	0.39	345
200	0.30	0.82	0.59	300

normally should be avoided if possible. All simulations were performed at an altitude of 3000 ft. The rotor forces and moments, which were computed based on the blade surface pressure, are converged after 11 loose coupling iterations (Ref. 32).

Total power validation

Figure 5 shows the total power comparison between the simulation results and available flight-test data (Ref. 15). Since the lift-offset values of the flight-test data were not documented, a lift-offset value of 0.2 was assumed for power validation. It was also assumed that the jet propulsion power can be estimated based on a propeller propulsive efficiency factor (η). Johnson (Ref. 7) calculated the auxiliary propulsion power of a heavy-lift coaxial rotorcraft based on the same assumption with $\eta = 0.9$. Jacobellis et al. (Ref. 9) also followed the same assumption to compute the total power of a notional XH-59A model. In this research, the total power of the coaxial configuration was approximated using the following equation:

$$P_{\text{total}} = P_{\text{upper}} + P_{\text{lower}} + \frac{T_{\text{aux}} \cdot V_\infty}{\eta} \tag{5}$$

where P_{total} is the total power, P_{upper} is the upper rotor power, P_{lower} is the lower rotor power, and T_{aux} is the thrust produced by auxiliary engines. $\eta = 0.9$, which was implemented by Johnson (Ref. 7) for the total power calculation of a lift-offset coaxial rotor, was also used throughout this research. The errors of the simulation results are within 7% of the flight-test data.

100 kt

The simulation results at 100 kt with lift offset equal to 0.0, 0.1, and 0.2 were first evaluated to investigate the effect of lift offset on the coaxial rotor acoustics. Figure 6(a) shows the isosurface of a non-scaled Q-criterion value ($\bar{Q} = 0.0001$) colored by vorticity magnitude

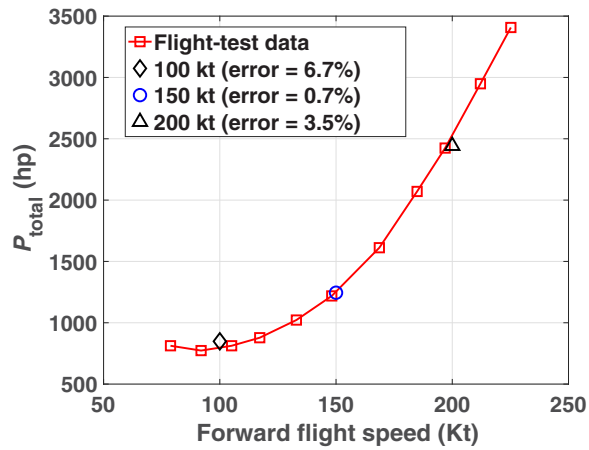

Fig. 5. Validation of total power.

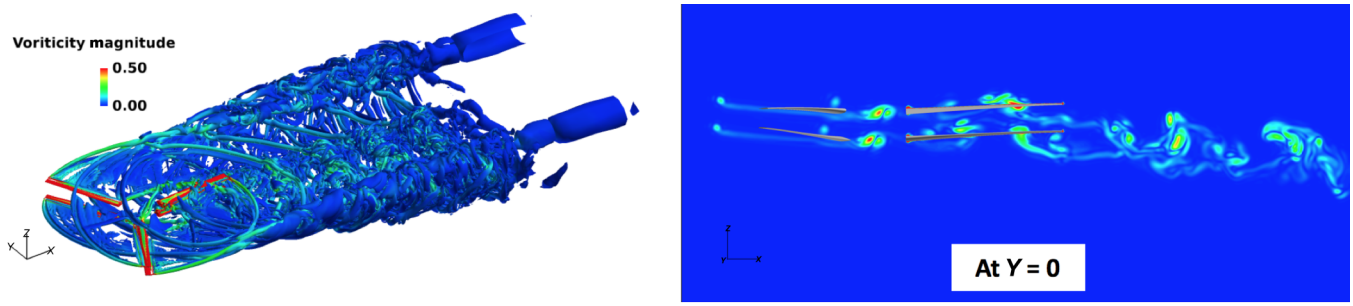

(a) 100 kt

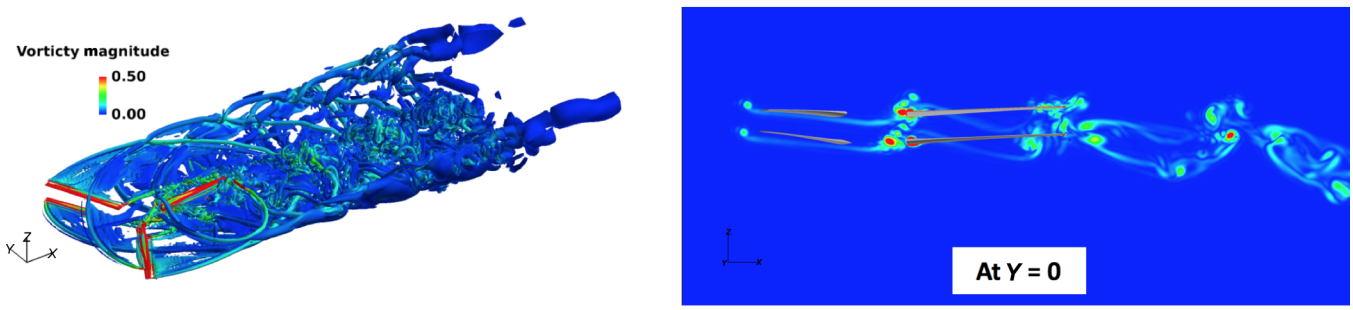

(b) 150 kt

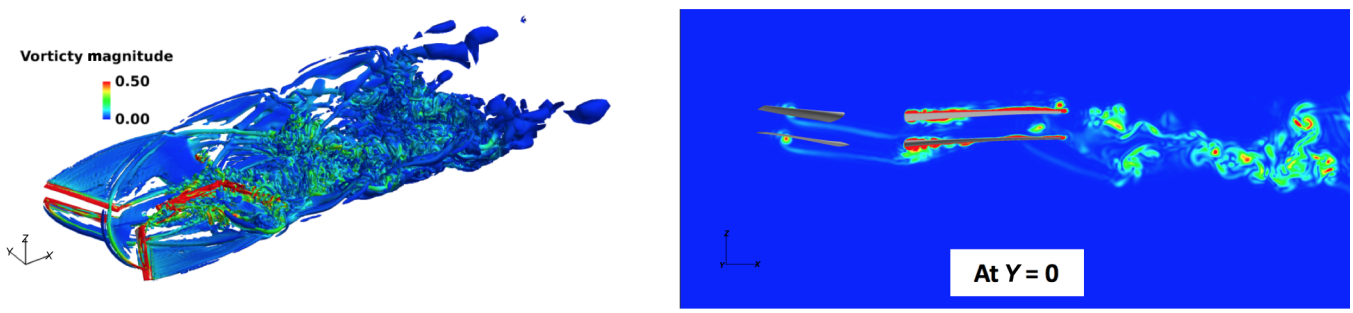

(c) 200 kt

Fig. 6. Isosurfaces of Q-criterion and vorticity contours at 100, 150, 200 kt with lift offset equal to 0.2.

at 100 kt with lift offset equal to 0.2. In this work, the Q-criterion was nondimensionalized by $(c/L_{\text{ref}})^2$, and the vorticity magnitude was nondimensionalized by c/L_{ref} in the near-body flow solver. The Q-criterion was evaluated using the following equation:

$$Q = \frac{1}{2}(||W_{ij}||^2 - ||S_{ij}||^2) \tag{6}$$

where W_{ij} is the spin-rate tensor and S_{ij} is the strain-rate tensor. No rotor-to-rotor BVI has been found from the isosurface contour and dynamic animation, as is expected because of the high rotor-wake convection rate during high-speed forward flight. Passe et al. (Ref. 33) pointed out that rotor-to-rotor interferences could be negligible at high speed during steady forward flight. Only self-BVIs, which imply the interactions between rotor tip vortices and the blades of the same rotor, were found. It should also be noted that the shaft angle of attack of this vehicle is at 0° since the rotor disk is not required to tilt forward to provide the propulsive force. Thus, unlike a conventional helicopter, this compound rotorcraft is likely to encounter self-BVIs at high speeds. Moreover, the aerodynamic and acoustic characteristics of the lift-offset coaxial rotor may vary depending on the shaft angle. Therefore, the results in this work may not always be the representative of the acoustics of a lift-offset coaxial rotor, although a zero shaft angle is common for most compound rotorcraft. Besides tip-induced BVIs, root-induced BVIs where blade–root vortices interact with the blades of the same rotor can be seen from the isosurface. However, these root-induced BVIs are only artifacts of the CFD simulation since the rotor blades are not physically attached to rotor hubs. Results are expected to be different in the presence of rotor hubs.

Figure 7 represents the azimuthal (time) derivative of sectional normal force of both upper (rotating in the counterclockwise direction) and lower (rotating in the clockwise direction) rotors of the coaxial rotor at lift offset equal to 0.0, 0.1, and 0.2. The azimuthal derivative of sectional normal force is considered as a direct source term of $\dot{l}_r$ in the loading noise acoustic pressure equation (Eq. (4)) of Farassat's Formulation 1A, which serves as an indicator of impulsive acoustic sources. The impulsive self-BVI events on the advancing sides of both upper and lower rotors near 50°, 70°, and 90° are visible in all lift-offset cases. The root-induced BVI events can also be seen near 20° of both upper and lower rotors. These self-BVI events in the first quadrants of both upper and lower rotors could lead to highly impulsive noise in acoustic prediction. Further,

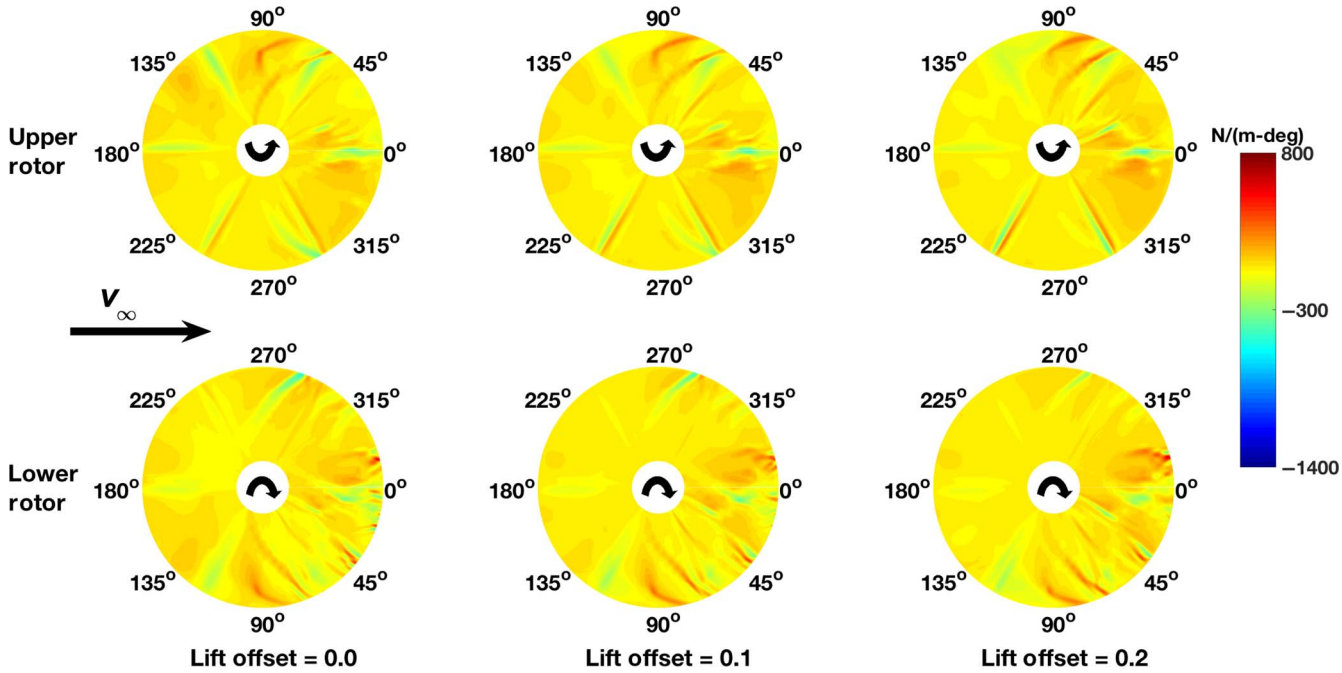

Fig. 7. Azimuthal derivative of sectional normal force at 100 kt.

the self-BVI events located on the retreating sides of the coaxial rotor near 280° or in the fourth quadrants are also apparent and are gradually reducing in strength with increasing lift offset. It is possible that the change of rotorcraft trim at higher lift offset causes both the trajectory and magnitude of this self-BVI to vary, which ultimately reduces the BVI strength. Unlike the self-BVI events located in the first quadrants, the self-BVI events in the fourth quadrants are relatively weak and almost indistinguishable at a lift offset value of 0.2.

The azimuthal derivative of sectional normal force ($dF_z/d\Omega$), a direct input to the loading noise calculation, as a function of rotor azimuth (Ψ) was also plotted at 75% span of both upper and lower rotors (see Fig. 8) for a quantitative comparison. As shown in Fig. 8(a), the magnitude of the first two BVI events located near 50° and 70° of the upper rotor is increased by 325% and 219%, respectively, as the lift-offset value increases from 0.0 to 0.2. The third BVI event near 90° of the upper rotor, on the other hand, is reduced by 68% as the lift-offset value increases from 0.0 to 0.2. Similar trend can also be seen from the lower rotor plot (see Fig. 8(b)). These changes in BVI strength are possibly due to a change of vortex trajectory. Though both the vortex strength and trajectory were not studied in this paper, they will be investigated thoroughly in future work to understand the detailed flow physics.

In addition to the self-BVI and root-induced BVI events, abrupt changes of sectional normal force at every 60° were discovered. These abrupt changes are induced by blade-crossover interactions, where the upper rotor blades are overlapped with the lower rotor blades. These interactions are more intensive in magnitude (see Figs. 7 and 8) on the upper rotor than on the lower rotor. The strength of the blade-crossover interactions also appears stronger on the retreating side of the

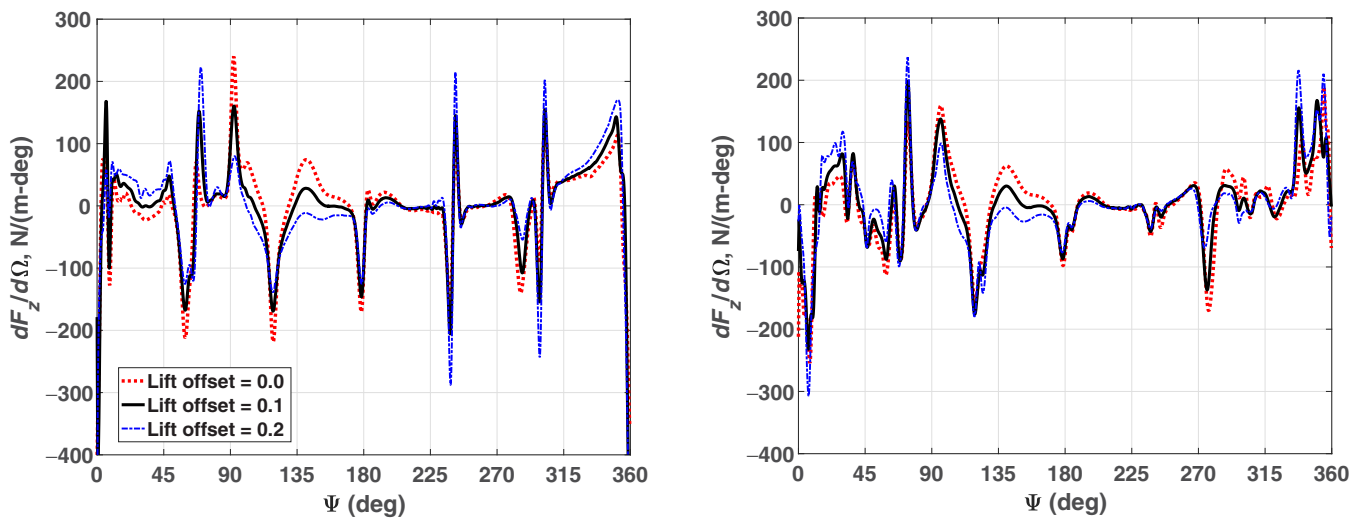

(a) Upper rotor **(b) Lower rotor**

Fig. 8. Azimuthal derivative of sectional normal force at 75% span at 100 kt.

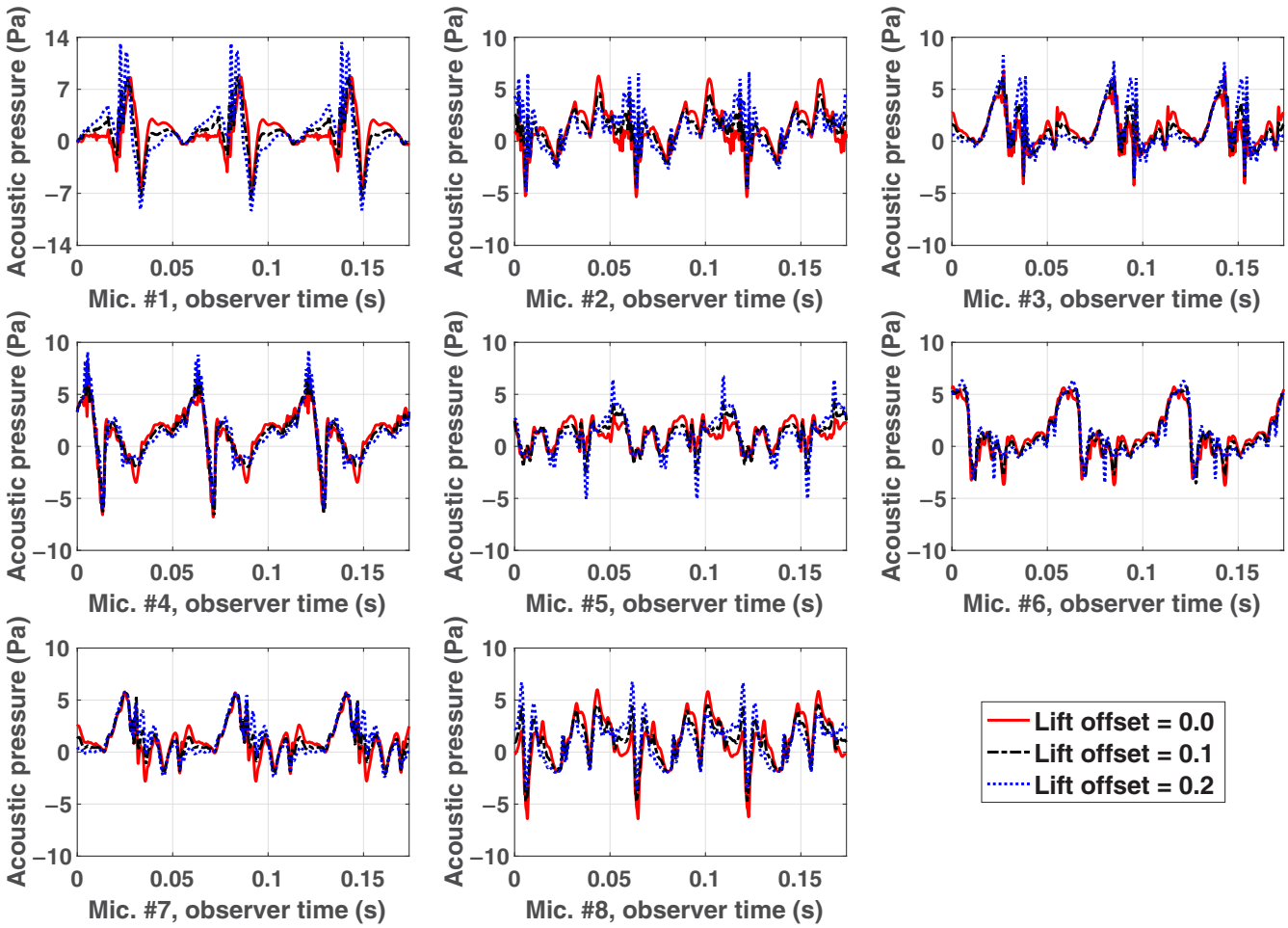

Fig. 9. Loading noise acoustic pressure at 100 kt with lift offset equal to 0, 0.1, and 0.2.

upper rotor than on the advancing side of the upper rotor. Moreover, Fig. 8 shows a significant increase in magnitude of the blade-crossover interactions on the retreating side of the upper rotor as the lift offset value increases. The percent difference of the peak values at 240° of the upper rotor (the blade-crossover event on the retreating side of the upper rotor) between the lift offset of 0.0 and 0.2 cases is approximately 110%. The strength of the blade-crossover events, however, is reduced on the advancing side of the upper rotor with increasing lift offset. The maximum peak value of the blade-crossover events is reduced by approximately 46% as the lift-offset value increases from 0.0 to 0.2. These physical patterns are possibly due to (1) the stronger influence of the suction side (upper surface of the blade) of the lower rotor blades has on the upper rotor than the pressure side (lower surface of the blade) of the upper rotor blades has on the lower rotor; (2) the reduction of separation distance between upper and lower rotor blades on the retreating side of the upper rotor, when the advancing side of the lower rotor flaps upward to produce additional lift and vice versa on the advancing side of the upper rotor. Following the CFD analysis, the acoustic characteristics of the coaxial rotor were studied.

Figure 9 shows the acoustic simulation results of loading noise acoustic pressure at 100 kt with lift offset equal to 0.0, 0.1, and 0.2. Since the magnitude of loading noise acoustic pressure has been found much larger than that of the thickness noise acoustic pressure, this paper primarily focuses on the analysis of loading noise. According to the results shown in Fig. 9, impulsive signals have been found at most microphone positions and could be induced by a combination of the self-BVI and blade-crossover events as shown in the polar plots of the azimuthal derivative of sectional normal force (see Fig. 7). However, microphones 2−4, which are located toward the advancing side of the lower rotor, show slightly higher impulsive signals with steeper positive and negative pressure peaks than microphones 6−8 that are positioned toward the advancing side of the upper rotor, possibly due to the stronger rotor–wake interaction near 0°.

At microphones 2−4, the advancing side of the lower rotor is thought to be an important noise source area due to the effect of Doppler amplification factor. Aerodynamic interactions on the advancing side of the upper rotor, on the other hand, is thought to influence microphones 6−8 the most. Recall the discussion of the Doppler amplification factor ($1/|1 - M_r|$) of Farassat's Formulation 1A under the section Acoustic Simulation Setup, the blade-tip Mach number is high on the advancing sides of the coaxial rotor, and could magnify the Doppler amplification factor, so that the advancing side of each rotor becomes a major acoustic source area with respect to microphone positions. For instance, the advancing blades of the lower rotor are moving toward microphones 2−4 with high tip Mach number. Thus, the Doppler amplification factor on the advancing side of the lower rotor is expected to be high at microphones 2−4.

Besides the effect of the Doppler amplification factor, the self-BVI and blade-crossover events located on the advancing side of each rotor, which are major sources of the term $\dot{l}_r$ in the loading noise equation of

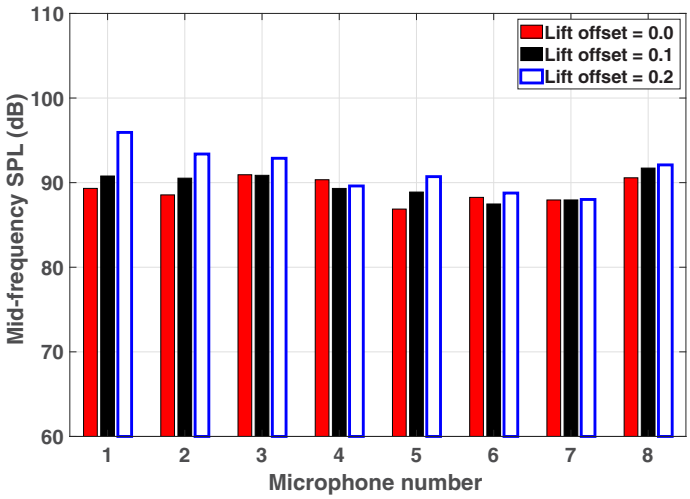

Fig. 10. Mid-frequency SPL comparison at 100 kt.

Farassat's Formulation 1A, could also strengthen the impulsive signals at microphones 2, 3, 4, 6, 7, and 8. Though the Doppler amplification is expected to be weak on the retreating side of the upper rotor due to low tip Mach number, the highly impulsive blade-crossover events located at 240° and 300° on the retreating side of the upper rotor may still contribute as minor acoustic sources to loading noise.

The effect of lift offset on acoustics was also analyzed based on Fig. 9. The case with lift offset equal to 0.2 shows sharper acoustic pressure pulses at most microphone locations, and this increase of acoustic pressure peaks could be thought as a direct outcome of the stronger rotor–wake interaction near 0° of the lower rotor, the self-BVI events in the first quadrants, and the blade-crossover events on the retreating side of the upper rotor. The reduction of negative acoustic pressure peaks at microphones 7 and 8 could be related to the reduced strength of the blade-crossover events on the advancing side of the upper rotor.

Furthermore, mid-frequency sound pressure level (SPL), which includes the contribution from both BVI and blade-crossover interactions at 100 kt, was also calculated by integrating the SPL spectrum from 10th to 50th blade harmonics to further demonstrate the influence of lift offset on acoustics. It is evident from Fig. 10 that mid-frequency SPL increases with increasing lift offset at almost all microphone positions except microphone 7, which also matches with the trend seen from the loading noise acoustic pressure plot.

150 kt

The acoustic characteristics of the coaxial rotor at 150 kt with lift offset equal to 0.2 was also studied. Figure 6(b) shows the isosurface of a nonscaled Q-criterion value ($\bar{Q} = 0.0001$) colored by vorticity magnitude at 150 kt. Other than self-BVIs, no trace of rotor-to-rotor BVI was detected. Again, self-BVIs, root-induced BVIs, and blade-crossover interactions can be seen at 150 kt from the polar contours of the azimuthal derivative of sectional normal force (see Fig. 11). In addition to the polar plots, Fig. 12 shows the azimuthal derivative of sectional normal force at 75% span. The self-BVI events of both upper and lower rotors are located near 60° and 90° in the first quadrants. The root-induced BVI events of the upper and lower rotors are positioned near 20° in the first quadrants. Other than the BVI events, blade-crossover interactions are located at every 60°, but are significantly more impulsive at 240° and 300° of the upper rotor. All of above aerodynamic interactions are considered as major acoustic sources.

Similar to the acoustic analysis performed at 100 kt, the loading noise acoustic pressure results at 150 kt were analyzed. Shown in Fig. 13, microphones 2−4 display steeper pressure peaks in comparison to microphones 6−8. The Doppler amplification factor is expected to be greatest on the advancing sides of both rotors and magnifies the strength of impulsive acoustic sources such as the self-BVI events located in the first quadrants of both rotors. Overall, the trend observed at 150 kt is identical to the pattern shown at 100 kt.

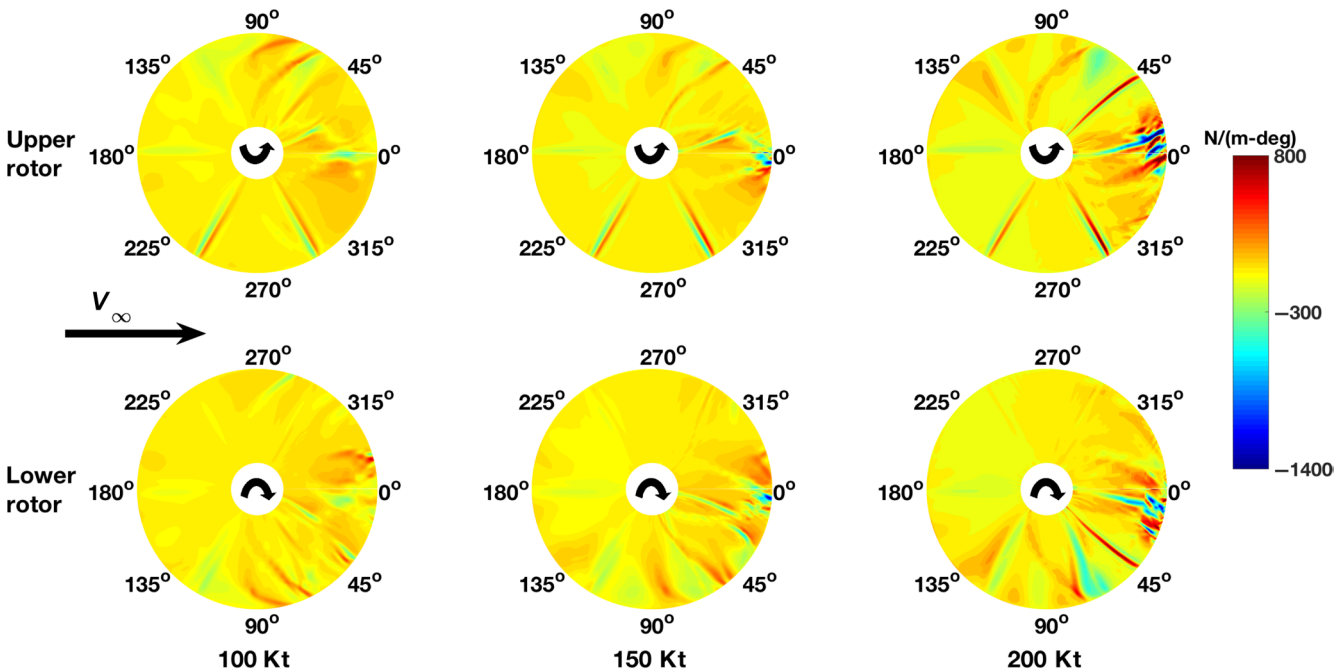

Fig. 11. Speed comparison (lift offset equal to 0.2) of the azimuthal derivative of sectional normal force.

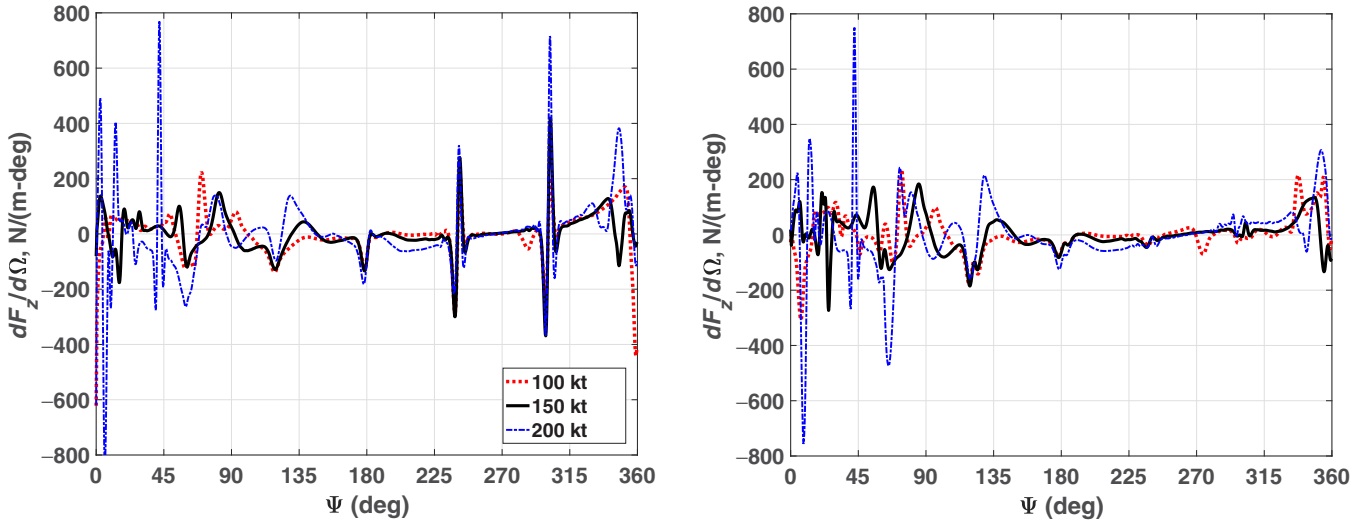

(a) Upper rotor (b) Lower rotor

Fig. 12. Azimuthal derivative of sectional normal force at 75% span at 100, 150, and 200 kt.

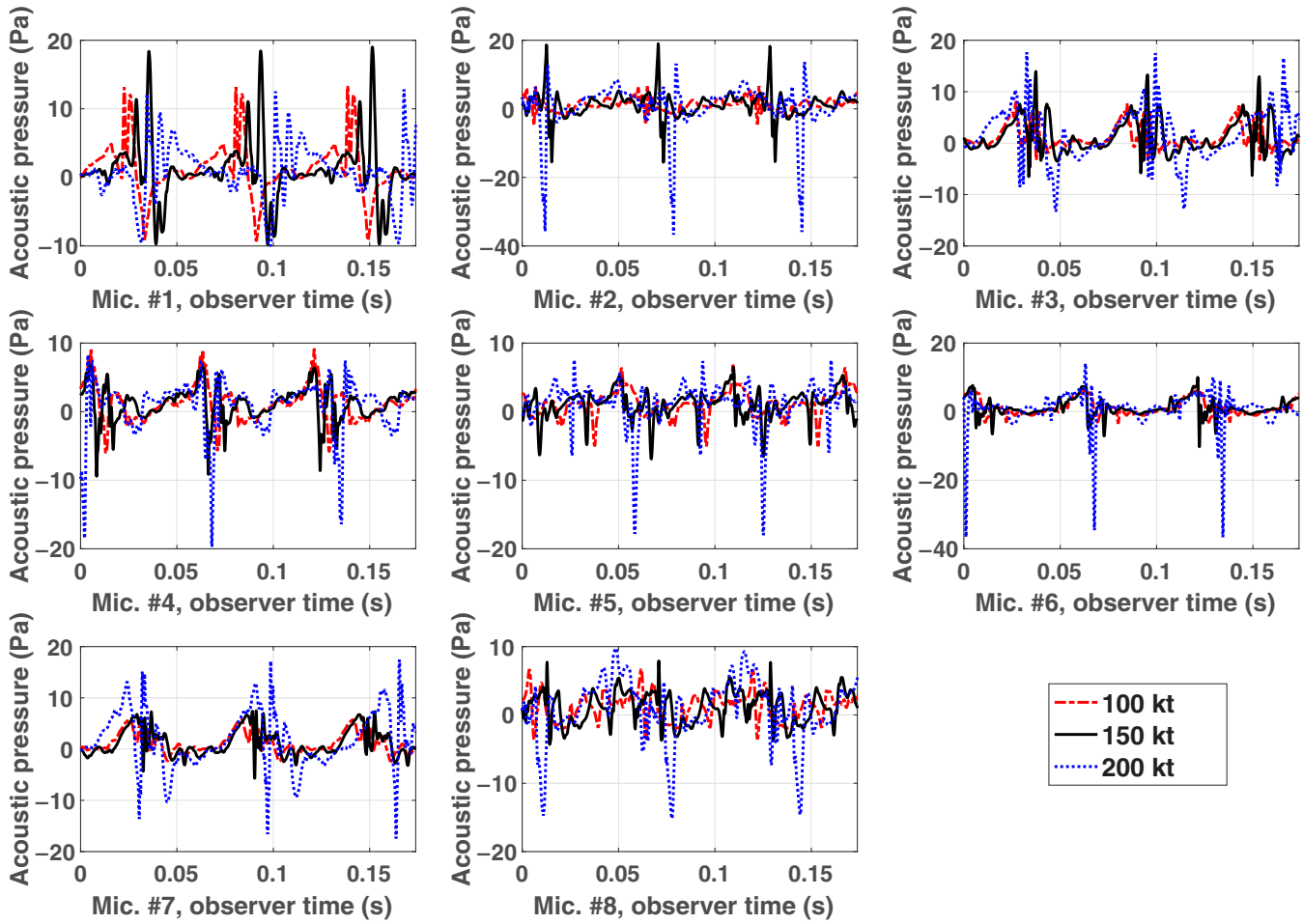

Fig. 13. Comparison of loading noise acoustic pressure at various speeds with lift offset equal to 0.2.

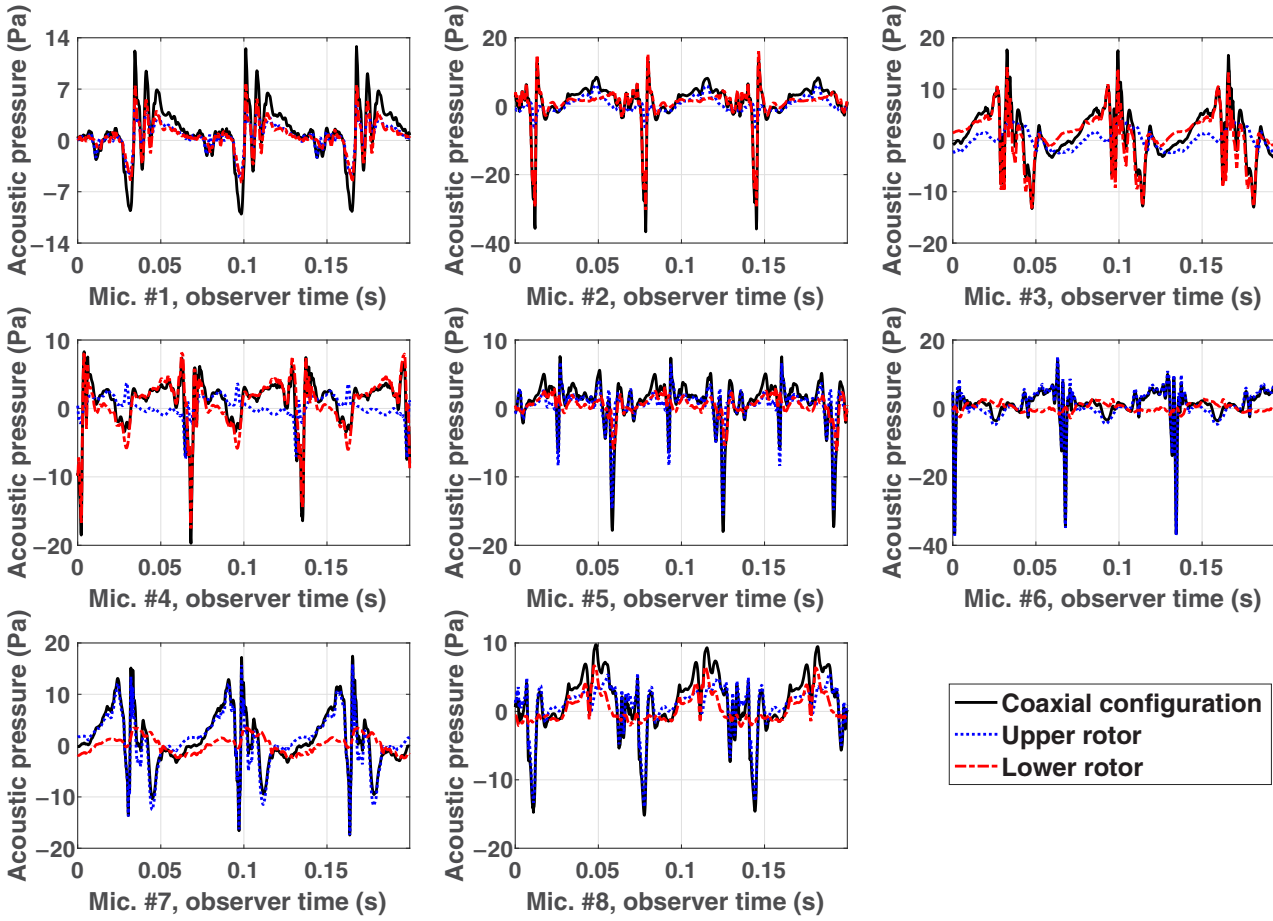

Fig. 14. Contributions of each rotor on loading noise acoustic pressure at 200 kt with lift offset equal to 0.2.

200 kt

A higher speed case at 200 kt with lift offset equal to 0.2 was also analyzed, and phenomena similar to the lower speed cases (100 and 150 kt) were observed. Figure 6(c) shows the isosurface of a nonscaled Q-criterion value ($\bar{Q} = 0.0001$) colored by vorticity magnitude at 200 kt. Self- and root-induced BVIs were observed from the isosurface. According to the 200-kt case of Fig. 11, self-BVI events are visible near 45° and 80° of both upper and lower rotors. Root-induced BVIs near 20° in the first quadrants as well as the blade-crossover interactions at every 60° can also be seen from the polar contours. Shown in Fig. 12, the strength of the first self-BVI events near 45° of both rotors is significantly higher than other aerodynamic interactions except the blade-crossover event located at 300° of the upper rotor. Unlike the two previous speed cases, the blade-crossover interaction located at 60° of the lower rotor is also considered as a strong source of impulsive noise. The area of this blade-crossover event is also relatively large when compared to other aerodynamic events (see the 200-kt case of Fig. 11). On the upper rotor, the blade-crossover events are once again visible on the retreating side. However, the blade-crossover interaction at 300° appears much stronger than the one at 240°. The blade–crossover interaction near 60° of the upper rotor (see the 200-kt case of Fig. 11) also becomes distinguishable on the polar plot at 200 kt.

The acoustic simulation results at 200 kt (see Fig. 13) were reviewed after identifying possible impulsive acoustic sources. Sharp positive and negative pressure peaks due to a combination of highly impulsive self-BVIs, root-induced BVIs, and blade-crossover interactions can be seen at all microphone positions. Because of the highly impulsive acoustic sources and Doppler amplification factor in the first quadrants of both upper and lower rotors, the negative pressure peaks are maximized at microphones 2 and 6. It is also expected that the strong root-induced BVI events near 20° and the rotor–wake interaction near 0° cause the magnitude of negative pressure peaks to rise at microphone 5.

Decomposition of the coaxial rotor at 200 kt

The loading noise acoustic pressure of the coaxial configuration was decomposed into two components: upper and lower rotors. This decomposition process was used to clarify the acoustic source contribution from each rotor. According to Fig. 14, the lower rotor at microphones 2−4 displays higher acoustic pressure peaks than the upper rotor. Since the advancing side of the lower rotor contributes higher magnitude of impulsive acoustic sources at microphones 2−4, the lower rotor is expected to be dominant at these microphones. Once again, the Doppler amplification factor is also expected to be high on the advancing side of the lower rotor and low on the retreating side of the upper rotor, which may explain why acoustic pressure pulses of the lower rotor are more impulsive than that of the upper rotor at these microphones. On the other hand, the advancing side of the upper rotor contributes greater sound sources at microphones 6−8. The same reasoning from the results seen at microphones

Microphones 2−4 can be applied to justify the upper rotor results at microphones 6−8. Though microphone 4 still shows narrow negative pressure pulses of the upper rotor, which could be the noise induced

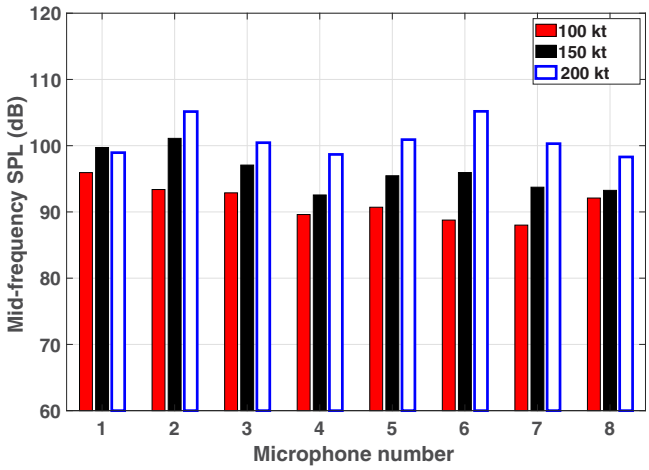

Fig. 15. Comparison of mid-frequency SPL between 100, 150, and 200 kt.

by the blade-crossover events located on the retreating side of the upper rotor, the strength is relatively weaker than the pressure peaks of the lower rotor. Moreover, the upper rotor shows larger negative pressure peaks at microphone 5 since both root-induced BVI and rotor–wake interaction near 0° of the upper rotor are significantly stronger than that of the lower rotor. Unlike other microphones, microphone 1 shows equivalent source contributions from both upper and lower rotors.

Effect of flight speed

As part of the parametric studies, the effect of forward flight speed on the strength of acoustic sources and far-field noise was performed by keeping the lift-offset value at 0.2. Figure 12 was used to illustrate the effect of flight speed. As the forward flight speed increases, the magnitude of self-BVIs increases significantly on the advancing sides of both upper and lower rotors. The percent difference between the BVI peak of the 200-kt case near 45° of the upper rotor and the BVI peak of the 100-kt case near 70° of the upper rotor is approximately 246%. The strength of the blade-crossover interactions also escalates notably on the retreating side of the upper rotor. The percent difference of the peak values near 300° (the blade-crossover event in the fourth quadrant of the upper rotor) between the 100- and 200-kt cases is approximately 258%.

Furthermore, the azimuthal positions of the first self-BVI events of both upper and lower rotors are shifted from 55° to 45° as the speed increases from 100 to 200 kt. The distance between the adjacent self-BVI events also becomes larger in the first quadrants of both upper and lower rotors according to Fig. 11. The shift in positions of the self-BVI events is due to higher rotor–wake convection rate at high speed. Figure 6 shows a comparison of scaled vorticity magnitude at the $Y = 0$ plane between the three speed cases. The rotor wake convects at a much slower rate in the downstream direction at 100 kt when compared to the 200-kt case. Because of the high wake convection rate, the number of self-BVI events in the first quadrants of both upper and lower rotors (see Fig. 11) is reduced from three to two as the speed increases from 100 to 150 kt. Additionally, the strength of root-induced vorticies near 20° gradually grows stronger with increasing speed and could lead to highly impulsive pressure pulses at microphone 5. These impulsive root-induced vorticies, as can be seen from Fig. 6, are merged with the rotor wake and lead to additional turbulence in the rotor–wake region especially at 200 kt.

Figure 13 shows a comparison of loading noise acoustic pressure at 100, 150, and 200 kt with lift offset equal to 0.2. It can be clearly seen that the strength of acoustic pressure pulses at most microphone positions except microphone 1 increases significantly with increasing speed, which is in conjunction with the observations made from the aerodynamic simulations. Different from other microphones, microphones 2 and 6 are influenced the most because they are positioned toward the advancing side of the lower rotor where the impulsive self-BVI events are evident. It should also be noticed that the difference between the 100- and 150-kt cases is smaller than the discrepancy between the 150- and 200-kt cases. Though the magnitude of the self-BVI events in the first quadrants of both upper and lower rotors is increased as the speed increases from 100

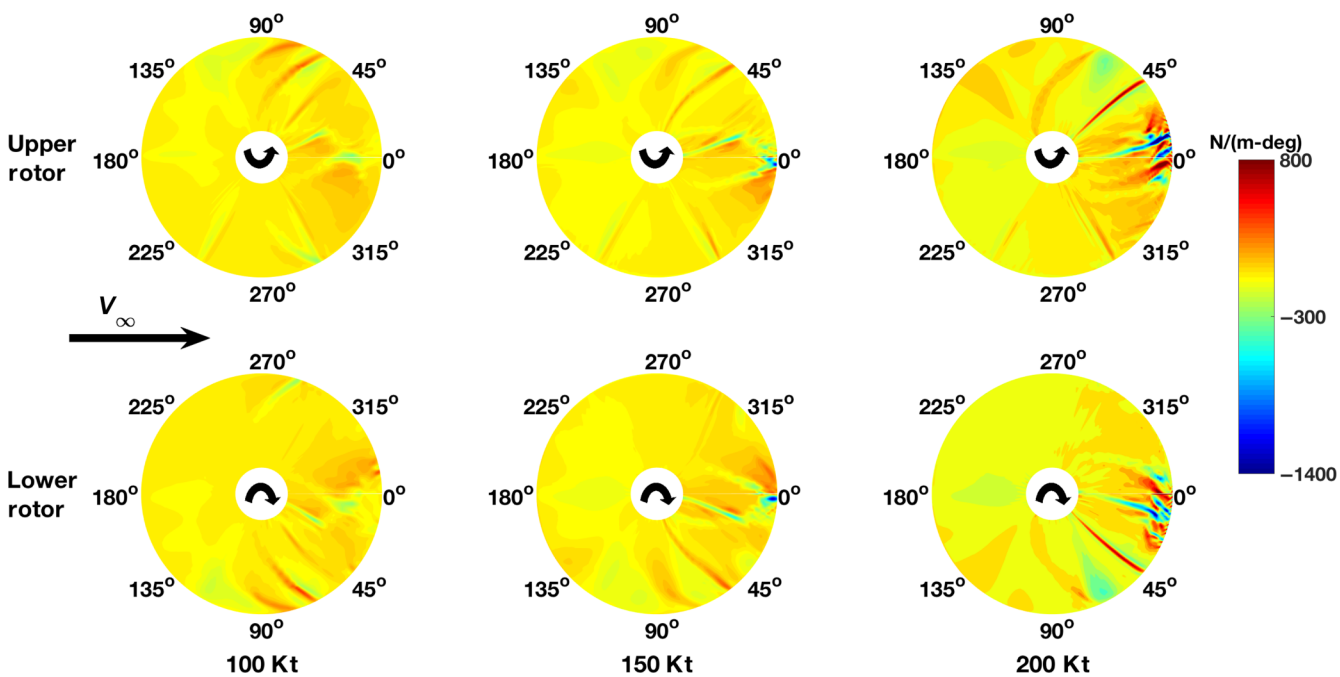

Fig. 16. Azimuthal derivative of sectional normal force at 100 kt with lift offset equal to 0.2 and separation distance equal to 1.14 m.

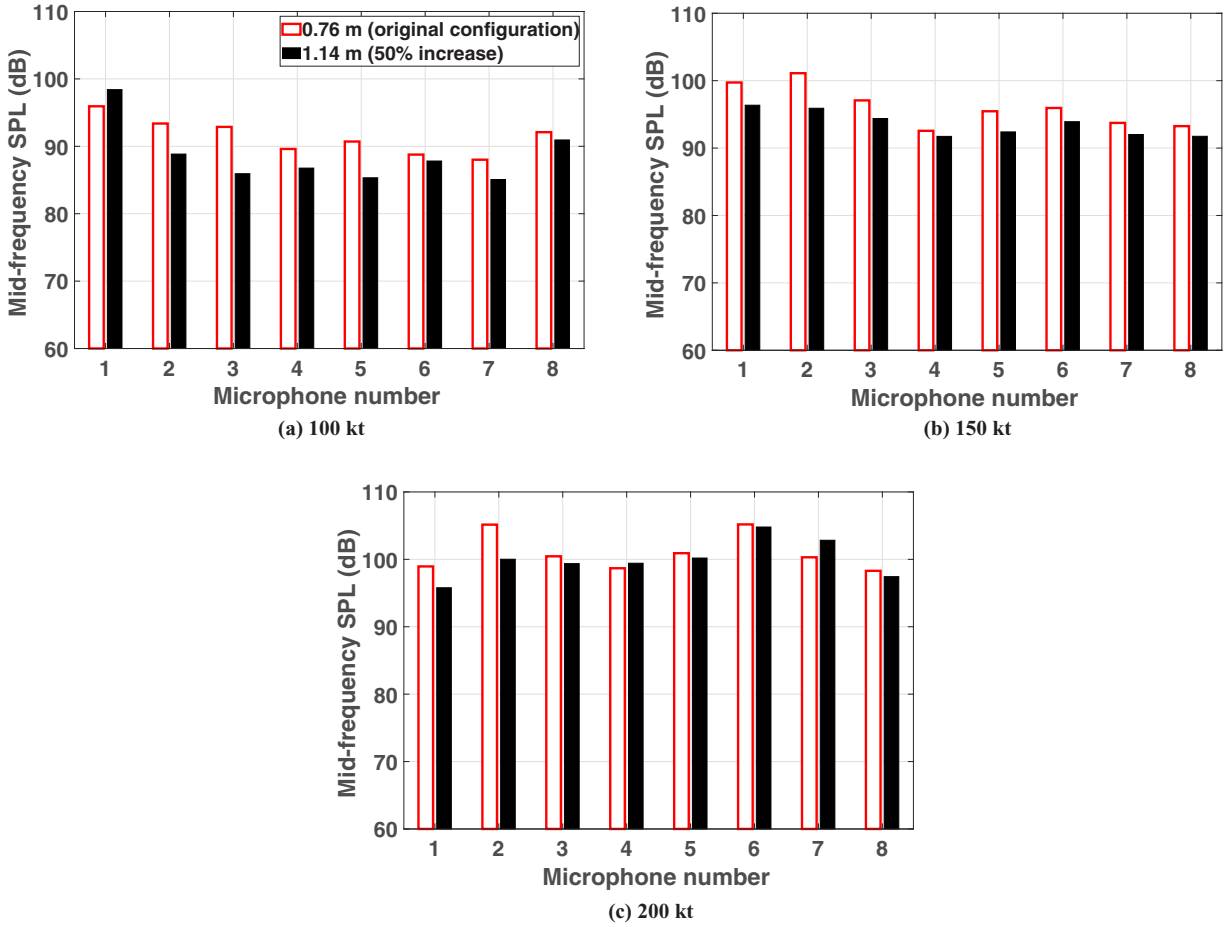

(a) 100 kt

(b) 150 kt

(c) 200 kt

Fig. 17. Mid-frequency SPL comparison for the parametric study of separation distance.

to 150 kt, the number of self-BVI events is reduced from three to two. It is possible that the boost in self-BVI strength is compensated for the reduction of the number of self-BVI events at 150 kt.

To demonstrate the effect of flight speed on acoustics, mid-frequency SPL was compared and shown in Fig. 15 at the eight microphone positions. The mid-frequency SPL results of the 200-kt case appear to be much higher than the lower speed cases at most microphone positions except microphone 1, which accords with the trend seen from the acoustic pressure plot or Fig. 13. The difference between the 100- and 200-kt cases can be as large as approximately 15 dB at microphone 6.

Effect of separation distance

The vertical separation distance between the upper and lower rotors of the lift-offset coaxial configuration is also considered as a key design parameter, which can affect both aerodynamics and acoustics of the vehicle. Therefore, a parametric study of rotor-to-rotor separation distance was conducted in this research at 100, 150, and 200 kt with lift offset equal to 0.2. The separation distance of the original coaxial configuration is increased by 50% or from 0.76 to 1.14 m. Figure 16 shows the polar contours of the azimuthal derivative of sectional normal force of the two cases: 0.76 m (original configuration) and 1.14 m (50% increase). The blade-crossover interactions originally located at 240° and 300° on the upper rotor become significantly weaker in magnitude and can hardly be seen. However, the blade–crossover interactions located in the first quadrants of both upper and lower rotors are still visible, especially at 200 kt. It should also be noted that there is a substantial reduction of rotor–wake interaction near 0° of the lower rotor at 100 kt. Besides the reduction of rotor–wake interaction, the strength of the self-BVI events located in the first quadrant of the lower rotor is slightly reduced with increasing separation distance when comparing Figs. 11 and 16. A change in induced velocity is thought to affect the vortex trajectory and cause the strength of self-BVIs to decrease as the separation distance increases. Further studies on both induced velocity and vortex trajectory should be performed. It should be seen from the mid-frequency SPL plots (see Fig. 17) that these reductions of aerodynamic interactions have led to acoustic mitigation.

At 100 kt (see Fig. 17(a)), a clear distinction between the two separation cases can be seen. Mid-frequency SPL is significantly reduced ranging from microphone 2 to microphone 7 with the largest reduction equal to approximately 8 dB at microphone 3. It is expected that the reduction of blade-crossover, self-BVI, and wake–blade interactions has led to noise alleviation. Unlike other microphones, microphone 8 is not significantly influenced by the separation distance since the aerodynamic interactions in the second quadrant of the upper rotor are weak in strength. More interestingly, the effect of separation distance does not tend to affect mid-frequency SPL at higher speeds (see Figs. 17(b) and 17(c)) by much at most microphone positions except microphone 2. Microphone 2 still shows a large reduction in mid-frequency SPL at 150 and 200 kt, where the largest difference is approximately 5 dB between the two separation cases, probably due to slightly weaker self-BVI and blade-crossover events. Unlike the 100-kt case, the

root-induced BVI, self-BVI, and blade-crossover events remain considerably strong in the first quadrants of both rotors at high speeds. Thus, the mid-frequency SPL reduction is expected to be lower at 150 and 200 kt than at 100 kt.

Conclusions

High-fidelity CFD/CSD loose coupling simulations at the three flight speeds—100, 150, and 200 kt—were performed to study the acoustics of a three-bladed lift-offset coaxial rotor in high-speed steady forward flight. The acoustic prediction tool PSU-WOPWOP was used to analyze acoustic data at eight microphone positions, which are positioned in a circle beneath the coaxial rotor. Parametric studies were also conducted to investigate the effect of lift offset, flight speed, and separation distance on rotor acoustics. The following conclusions have been drawn from the results discussed in this paper:

1) The total power computed based on the propeller efficiency assumption is within 7% error of the available flight-test data.

2) Both self-BVI and blade-crossover interactions are the most dominant aerodynamic interactions induced by a lift-offset coaxial rotor in high-speed forward flight at a zero shaft angle. Nonphysical root-induced BVI also appears to be a strong acoustic source at high speed, but its effect on acoustics should be different in the presence of a coaxial rotor hub.

3) The strength of self-BVI and blade-crossover interactions are heavily dependent on the lift offset value and forward flight speed. These aerodynamic interactions have increased substantially with increasing lift offset and forward flight speed.

4) Mid-frequency SPL shows that higher lift offset can increase the total noise up to 6 dB.

5) The magnitude of mid-frequency SPL is more sensitive to the rotor-to-rotor separation distance at a lower speed than at a higher speed. Mid-frequency SPL becomes significantly lower as much as 8 dB for the 100-kt case with larger separation distance than the original model. At 200 kt, the difference between the two separation cases is relatively small mainly due to less rotor–wake interaction.

Though the acoustic characteristics of the lift-offset coaxial rotor have been studied using high-fidelity simulation tools at various lift-offset values, flight speeds, and separation distances, the flow physics are not thoroughly studied. Both tip vortex strength and trajectory should be investigated to better understand the fundamental physics of noise sources. A further study to quantify the relative importance between BVI noise and blade-crossover interaction noise is recommended for future research. Additionally, the shaft angle-of-attack could sbe another key parameter to investigate, since it could largely change the BVI events in terms of magnitude and location and also the associated acoustics.

Acknowledgments

This research was partially funded by the U.S. Government under Agreement No. W911W6-17-2-0003. The U.S. Government is authorized to reproduce and distribute reprints for Government purposes notwithstanding any copyright notation thereon. The views and conclusions contained in this document are those of the authors and should not be interpreted as representing the official policies, either expressed or implied, of the Aviation Development Directorate or the U.S Government. The authors would like to thank Roger Strawn from the U.S. Army Aviation Development Directorate (ADD) for providing the DoD High Performance Computing (HPC) resources and summer internship for the first author; Mark Potsdam, Jain Rohit, Beatrice Roget, and Wel Chong (Ben) Sim from ADD for their insightful advice and assistance on learning Helios; and Neal Chanderjian and Williams Chan from NASA Ames for their technical advice on rotorcraft simulation and mesh generation.

References

[1]Ruddell, A. J., and Marcrino, J. A., "Advancing Blade Concept (ABC) High Speed Development," Proceedings of the American Helicopter Society 36th Annual Forum, Washington, DC, May 13–15, 1980.

[2]Burgess, R. K., "The ABC™ Rotor—A Historical Perspective," Proceedings of the American Helicopter Society 60th Annual Forum, Baltimore, MD, June 7–10, 2004.

[3]Cheney, M. C., "The ABC Helicopter," AIAA 69-217, Proceedings of the AIAA/AHS VTOL Research, Design, and Operations Meeting, Atlanta, GA, February 17–19, 1969.

[4]Paglino, V. M., "Forward Flight Performance of a Coaxial Rigid Rotor," Proceedings of the American Helicopter Society 27th Annual Forum, Washington, DC, May 19–21, 1971.

[5]Walsh, D., Weiner, K., Arifian, K., Lawrence, T., Wilson, T., Millott, T., and Blackwell, R., "High Airspeed Testing of the Sikorsky X2 Technology™ Demonstrator," Proceedings of the American Helicopter Society 67th Annual Forum, Virginia Beach, VA, May 4, 2011.

[6]Bowles, P. O., Matalanis, C., Battisti, M., Min, B., Wake, B. E., Tuozzo, N., and Lorber, P. F., "Full-Configuration CFD Analysis of the S-97 RAIDER™," Proceedings of the Vertical Flight Society 75th Annual Forum, Philadelphia, PA, May 13–16, 2019.

[7]Johnson, W., "Influence of Lift Offset on Rotorcraft Performance," NASA TP-2009-215404, November 2009.

[8]Yeo, H., and Johnson, W., "Investigation of Maximum Blade Loading Capability of Lift-Offset Rotors," *Journal of the American Helicopter Society*, **59**, 012005 (2014). doi:10.4050/JAHS.59.012005.

[9]Jacobellis, G., Gandhi, F., and Floros, M., "Using Control Redundancy for Power and Vibration Reduction on a Coaxial Helicopter at High Speeds," *Journal of the American Helicopter Society*, **64**, 032008 (2019). doi:10.4050/JAHS.64.032008.

[10]Hirschberg, M., "Joint Multi-Role Moves Forward: Four Teams Begin JMR Phase 1 Air Vehicle Demonstration," *Vertiflight*, Vol. 60, (1), January–February 2014, pp. 24–27.

[11]Kim, H. W., Duraisamy, K., and Brown, R., "Aeroacoustics of a Coaxial Rotor in Level Flight," Proceedings of the American Helicopter Society 64th Annual Forum, Montréal, Canada, April 29–May 1, 2008.

[12]Walsh, G., Brentner, S. B., Jacobellis, G., and Gandhi, F., "An Acoustic Investigation of Coaxial Helicopter in High-Speed Flight," Proceedings of the American Helicopter Society 72nd Annual Forum, West Palm Beach, FL, May 17–19, 2016.

[13]Saberi, H., Khoshlahjeh, M., Ormiston, R., and Rutkowski, M., "Overview of RCAS and Application to Advanced Rotorcraft Problems," Proceedings of the American Helicopter Society Fourth Decennial Specialists Conference on Aeromechanics, San Francisco, CA, January 21–23, 2004.

[14]Schatzman, N. L., Komerath, M., and Romander, E. A., "Time-Varying Loads of Co-Axial Rotor Blade Crossings," *SAE International Journal of Aerospace*, Vol. 10, (2), December 2017, pp. 68–76.

[15]Ruddell, A. J., "XH-59A ABC Technology Demonstrator Altitude Expansion and Operational Tests," Technical Report USAAVRADCOM-TR-81-D-35, U.S. Army Research and Technology Laboratories (AVRADCOM), December 1981.

[16]Chan, W. M., "Enhancements to the Grid Generation Script Library and Post-Processing Utilities in Chimera Grid Tools," Proceedings of the 9th Symposium on Overset Composite Grid and Solution Technology, State College, PA, October 14–16, 2008.

[17]Chan, W. M., Rogers, S. E., Pandya, S. A., Kao, D. L., Buning, P. G., Meakin, R. L., Boger, D. A., and Nash, S. M., *Chimera Grid Tools User's Manual*, V. 2.1, NASA Ames Research Center, Moffett Field, CA, 2010.

[18]Chanderjian, N. M., "Advances in Rotor Performance and Turbulent Wake Simulation Using DES and Adaptive Mesh Refinement," ICCFD 3506, Proceedings of the 7th International Conference on Computational Fluid Dynamics, Big Island, HI, July 9–13, 2012.

[19]Chanderjian, N. M., "Naiver–Stokes Simulation of UH-60A Rotor/Wake Interaction Using Adaptive Mesh Refinement," Proceedings of the American Helicopter Society 73rd Annual Forum, Fort Worth, TX, May 9–11, 2017.

[20]Wissink, A. M., Kamkar, S., Pulliam, T., Sitaraman, J., and Sankaran, V., "Cartesian Adaptive Mesh Refinement for Rotorcraft Wake Resolution," AIAA 2010-4554, Proceedings of the 28th AIAA Applied Aerodynamics Conference, Chicago, IL, June 28–July 1, 2010.

[21]Wissink, A., Potsdam, M., Jain, R., Leffell, J., Jayaraman, B., Roget, B., Lakshminaravan, V., Forsythe, J., Sitaraman, J., and Bauer, A., "Improvements in the Helios Rotorcraft Simulation Code," Proceedings of the American Helicopter Society 72nd Annual Forum, West Palm Beach, FL, May 17–19, 2016.

[22]Felker, F. F., III, "Performance and Loads Data from a Wind Tunnel Test of a Full-Scale, Coaxial, Hingeless Rotor Helicopter," NASA TM-81329, October 1981.

[23]Nichols, R., Tramel, R., and Buning, P., "Solver and Turbulence Model Upgrades to OVERFLOW 2 for Unsteady and High-Speed Flow Applications," AIAA 2006-2824, Proceedings of the 25th AIAA Applied Aerodynamics Conference, San Francisco, CA, June 5–8, 2006.

[24]Spalart, P. R., and Allmaras, S. R., "A One-Equation Turbulence Model for Aerodynamics Flows," AIAA 92-0439, Proceedings of the 30th AIAA Aerospace Sciences Meeting and Exhibit, Reno, NV, Jan. 6–9, 1992.

[25]Spalart, P. R., Deck, S., Shur, M. L., Squires, K. D., Strelets, M. K., and Travin, A., "A New Version of Detached-Eddy Simulation, Resistant to Ambiguous Grid Densities," *Theoretical and Computational Fluid Dynamics*, Vol. 20, (3), July 2006, pp. 181–195.

[26]Potsdam, M., Yeo, Hyeonsoo, and Johnson, W., "Rotor Airloads Prediction Using Loose Aerodynamic/Structural Coupling," *Journal of Aircraft*, Vol. 43, (3), May–June 2006, pp. 732–742.

[27]Brentner, K. S., Brès, G. A., Perez, G., and Jones, H. E., "Maneuvering Rotorcraft Noise Prediction: A New Code for a New Problem," Proceedings of the American Helicopter Society Aerodynamics, Acoustics, and Test and Evaluation Technical Specialist Meeting, San Francisco, CA, January 13–25, 2002.

[28]Lee, S., Brentner, K. S., Farassat, F., and Morris, P. J., "Analytic Formulation and Numerical Implementation of an Acoustic Pressure Gradient Prediction," *Journal of Sound and Vibration*, Vol. 319, (3–5), January 2009, pp. 1200–1221.

[29]Brentner, K. S., and Farassat, F., "Modeling Aerodynamically Generated Sound of Helicopter Rotors," *Progress in Aerospace Sciences*, Vol. 39, (2–3), February–April 2003, pp. 83–120.

[30]Farassat, F., and Succi, G. P., "The Prediction of Helicopter Discrete Frequency Noise," *Vertica*, Vol. 7, (4), 1983, pp. 309–320.

[31]Ffowcs Williams, J. E., and Hawkings, D. L., "Sound Generation by Turbulence and Surface in Arbitrary Motion," *Philosophical Transactions of the Royal Society*, Series A, Vol. 264, (1151), May 1969, pp. 321–342.

[32]Jia, Z., Lee, S., and Brentner K. S., "Assessment of Turbulence Modeling and Wake-Grid Resolution for Lift-Offset Coaxial Rotor Simulations," AIAA 2018-4120, Proceedings of the 36th AIAA Applied Aerodynamic Conference, Atlanta, GA, June 25–29, 2018.

[33]Passe, B., Sridharan, A., and Baeder, J., "Computational Investigation of Coaxial Rotor Interaction Aerodynamics in Steady Forward Flight," AIAA 2015-2883, Proceedings of the 33rd AIAA Applied Aerodynamic Conference, Dallas, TX, June 22–26, 2015.